Instability of Poiseuille flow at extreme Mach numbers: Linear analysis and simulations

Zhimin Xie* and Sharath S. Girimaji

Department of Aerospace Engineering, Texas A&M University, College Station, Texas 77843-3141, USA

(Received 8 October 2013; revised manuscript received 10 January 2014; published 1 April 2014)

We develop the perturbation equations to describe instability evolution in Poiseuille flow at the limit of very high Mach numbers. At this limit the equation governing the flow is the pressure-released Navier-Stokes equation. The ensuing semianalytical solution is compared against simulations performed using the gas-kinetic method (GKM), resulting in excellent agreement. A similar comparison between analytical and computational results of small perturbation growth is performed at the incompressible (zero Mach number) limit, again leading to excellent agreement. The study accomplishes two important goals: it (i) contrasts the small perturbation evolution in Poiseuille flows at extreme Mach numbers and (ii) provides important verification of the GKM simulation scheme.

DOI: 10.1103/PhysRevE.89.043001 PACS number(s): 47.20.−k, 47.27.ek

I. INTRODUCTION

Couette and Poiseuille flows are prototypical shear flows in which many fundamental physical features of practical importance pertaining to instability, transition, and turbulence can be investigated. Both flows describe fluid motion between two parallel plates but driven in different ways. In a Couette flow, the bottom plate is stationary, and the top plate moves at a uniform velocity. The resulting flow has a linear velocity profile which corresponds to uniform shear (velocity gradient). The walls of a Poiseuille flow are stationary, and the fluid between them is driven by an applied uniform pressure gradient. The Poiseuille velocity profile is parabolic, and correspondingly, the shear varies in space. In computer simulations, the Couette flow away from the wall can be approximated as a homogeneous shear flow. Instability and turbulence in homogeneous shear flow have been extensively studied in the literature. Most recently, the instability characteristics of homogeneous shear flows at extreme values of Mach number have been contrasted in [1,2]. In that same vein, the main objective of this study is to examine the stability of Poiseuille flow at the two extremes of Mach-number-incompressible and highly compressible limits. In engineering literature, the Poiseuille flow is also called the channel flow. The main distinguishing feature between the two extreme limits of Poiseuille or channel flow is the action of pressure.

Pressure plays a profound role in shaping the nature of instability, transition, and turbulence phenomena in fluid flows. The interaction between pressure and velocity fields depends upon the flow-to-acoustic (pressure) time scale ratio quantified by the Mach number. At the vanishing Mach number limit, pressure evolves very rapidly to impose the incompressibility constraint on the velocity field. Under these conditions, hydrodynamic pressure can be completely determined from a Poisson equation. In such incompressible flows, pressure-enabled energy redistribution mitigates instability in hyperbolic flows but initiates and sustains instability in elliptic flows [3]. The flow physics at low Mach numbers is described by the incompressible Navier-Stokes equations.

With increasing Mach number, the nature of pressure action on the flow field changes. Pressure evolves according to a wave equation resulting from the energy conservation statement and the thermodynamic state equation. In high speed flows, as the time scales of velocity and pressure become comparable, pressure does not act rapidly enough to impose the divergence-free constraint on the velocity field. This in turn leads to the flow becoming compressible with significant changes in density across the field. At the limit of a very high Mach number, pressure evolution is very slow compared to that of the velocity field. Consequently, the velocity field evolves nearly imperviously to the pressure field. The pressureless Navier-Stokes equation, called the pressure-released equation (PRE), describes the evolution at extremely high Mach numbers. The PRE flow behavior has been shown to accurately characterize the high Mach number Navier-Stokes physics in homogeneous shear (Couette) flows [1,2,4]. The PRE equation has also been widely used to infer velocity gradient dynamics at very high Mach numbers [5].

In this study, we will perform a linear perturbation analysis of the PRE to describe the evolution of small perturbations in very high Mach number Poiseuille flows. At the limit of a very small Mach number, the classical Orr-Sommerfeld analysis is used to evaluate perturbation evolution. In addition to the analyses, direct numerical simulations (DNS) of the Poiseuille flow at extreme Mach numbers will be performed using the gas-kinetic method (GKM). Apart from providing insight into the instability flow physics at extreme Mach numbers, the present study has an important second goal to benchmark the validity of the GKM simulations at these limits.

The study can be broken down into four parts: (i) formulate and solve the linearized PRE for describing velocity perturbation evolution in high Mach number Poiseuille flow, (ii) contrast the high and low Mach number Poiseuille flow instability characteristics, (iii) perform (GKM) numerical simulations of instability evolution at these extreme Mach numbers, and (iv) compare the analytical and numerical results for mutual verification.

The paper is organized as follows. Section II contains the fundamental governing equations and linear analyses at the two Mach number limits. The GKM numerical scheme is described in Sec. III. Details of the simulations are also given.

*denver318@tamu.edu

A comparison between the analysis and numerical results is shown in Sec. IV. The paper concludes in Sec. V with a brief discussion.

II. GOVERNING EQUATIONS AND LINEAR ANALYSIS

In this section, we present the linear analysis of small perturbation evolution at both high and low Mach number limits. The compressible Navier-Stokes equations along with the ideal-gas assumption form the basis of our analysis.

$$\frac{\partial \rho^*}{\partial t^*} + \frac{\partial}{\partial x_j^*}(\rho^* u_j^*) = 0, \tag{1}$$

$$\frac{\partial u_i^*}{\partial t^*} + u_j^* \frac{\partial u_i^*}{\partial x_j^*} = \frac{1}{\rho^*} \frac{\partial \tau_{ij}^*}{\partial x_j^*}, \tag{2}$$

$$\rho^* c_v^* \left(\frac{\partial T^*}{\partial t^*} + u_j^* \frac{\partial T^*}{\partial x_j^*} \right) = \frac{\partial}{\partial x_j^*} \left(k^* \frac{\partial T^*}{\partial x_j^*} \right) + \tau_{ij}^* e_{ij}^*, \tag{3}$$

$$P^* = \rho^* R T^*. \tag{4}$$

The rate of strain tensor and stress tensor are defined as

$$e_{ij}^* = \frac{1}{2} \left(\frac{\partial u_i^*}{\partial x_j^*} + \frac{\partial u_j^*}{\partial x_i^*} \right), \tag{5}$$

$$\tau_{ij}^* = 2\mu^* e_{ij}^* + \left[\frac{2}{3}(\lambda^* - \mu^*) e_{kk}^* - P^* \right] \delta_{ij}, \tag{6}$$

where asterisks denote dimensional quantities, c_v^* is the specific heat at constant volume, k^* is the coefficient of thermal conductivity, R is the specific gas constant, μ^* is the coefficient of dynamic viscosity, and λ^* is the coefficient of second viscosity. The dynamic viscosity is assumed to follow Sutherland's law [6].

The equations are nondimensionalized with the following reference quantities: density ρ_0, velocity U_0, temperature T_0, characteristic length L, viscosity μ_0, heat conductivity k_0, and speed of sound a_0. The specific values of these quantities depend on the flow under consideration. For the channel flow, the reference values are those of background flow at the centerline at $t = 0$. L is half channel width. The dimensionless quantities are defined as

$$\begin{aligned} &\rho = \rho^*/\rho_0, \quad u_i = u_i^*/U_0, \; T = T^*/T_0, \\ &P = P^*/\rho_0 a_0^2, \quad x_i = x_i^*/L, \; t = U_0 t^*/L, \\ &\mu = \mu^*/\mu_0, \quad \lambda = \lambda^*/\mu_0, \; k = k^*/k_0. \end{aligned} \tag{7}$$

The dimensionless compressible Navier-Stokes (NS) equations can be rewritten as follows:

$$\begin{aligned} &\frac{\partial \rho}{\partial t} + \frac{\partial}{\partial x_j}(\rho u_j) = 0, \\ &\frac{\partial u_i}{\partial t} + u_j \frac{\partial u_i}{\partial x_j} = -\frac{1}{\rho} \frac{\partial P}{\partial x_i} \frac{1}{M^2} + \frac{\mu}{\rho} \frac{\partial^2 u_i}{\partial x_j \partial x_j} \frac{1}{\mathrm{Re}} \\ &\qquad + \frac{\mu + 2\lambda}{3\rho} \frac{\partial^2 u_j}{\partial x_i \partial x_j} \frac{1}{\mathrm{Re}}. \end{aligned} \tag{8}$$

The pressure equation is

$$\begin{aligned} &\frac{\partial P}{\partial t} + u_j \frac{\partial P}{\partial x_j} \\ &= \frac{\partial}{\partial x_j} \left(\frac{k}{\rho} \frac{\partial P}{\partial x_j} - \frac{kP}{\rho^2} \frac{\partial \rho}{\partial x_j} \right) \frac{\gamma}{\mathrm{RePr}} \\ &\quad + \frac{1}{2}\mu \left(\frac{\partial u_i}{\partial x_j} \frac{\partial u_i}{\partial x_j} + 2 \frac{\partial u_i}{\partial x_j} \frac{\partial u_j}{\partial x_i} + \frac{\partial u_j}{\partial x_i} \frac{\partial u_j}{\partial x_i} \right) \\ &\quad \times \frac{\gamma(\gamma - 1) M^2}{\mathrm{Re}} \\ &\quad + \frac{2}{3}(\lambda - \mu) \frac{\partial u_j}{\partial x_j} \frac{\partial u_k}{\partial x_k} \frac{\gamma(\gamma - 1) M^2}{\mathrm{Re}} - P \frac{\partial u_k}{\partial x_k} \gamma. \end{aligned} \tag{9}$$

The relevant dimensionless parameters are Reynolds number Re, Mach number M, Prandtl number Pr, and specific heat ratio γ:

$$\mathrm{Re} = \frac{\rho_0 U_0 L}{\mu_0}, \quad M = \frac{U_0}{a_0}, \quad \mathrm{Pr} = \frac{c_p^* \mu_0}{k_0}, \quad \gamma = \frac{c_p^*}{c_v^*}. \tag{10}$$

In the DNS simulations the Prandtl number Pr is held constant at 0.7. The specific heat ratio γ is held constant at 1.4.

A. High Mach number linear analysis

While the DNS performed in this work employs the full equation set, the analysis is restricted to inviscid (and nonconducting) flow phenomena. The simplified equations are

$$\frac{\partial \rho}{\partial t} + \frac{\partial}{\partial x_j}(\rho u_j) = 0, \tag{11}$$

$$\frac{\partial u_i}{\partial t} + u_j \frac{\partial u_i}{\partial x_j} = -\frac{1}{\rho} \frac{\partial P}{\partial x_i} \frac{1}{M^2}, \tag{12}$$

$$\frac{\partial P}{\partial t} + u_j \frac{\partial P}{\partial x_j} = -P \frac{\partial u_k}{\partial x_k} \gamma. \tag{13}$$

To investigate flow stability, we examine the small perturbation evolution. We decompose the flow field into background flow and perturbation quantities:

$$\rho = \bar{\rho} + \rho', \quad u_i = \bar{u}_i + u_i', \quad P = \bar{P} + P'. \tag{14}$$

The background flow equations have a form that is similar to that of total flow:

$$\frac{\partial \bar{\rho}}{\partial t} + \frac{\partial}{\partial x_j}\left(\bar{\rho} \bar{u}_j\right) = 0, \tag{15}$$

$$\frac{\partial \bar{u}_i}{\partial t} + \bar{u}_j \frac{\partial \bar{u}_i}{\partial x_j} = -\frac{1}{\bar{\rho}} \frac{\partial \bar{P}}{\partial x_i} \frac{1}{M^2}, \tag{16}$$

$$\frac{\partial \bar{P}}{\partial t} + \bar{u}_j \frac{\partial \bar{P}}{\partial x_j} = -\bar{P} \frac{\partial \bar{u}_k}{\partial x_k} \gamma. \tag{17}$$

The perturbation evolution equation can be obtained by subtracting the background flow equations (15)–(17) from the

corresponding full equations (11)–(13):

$$\frac{\partial \rho'}{\partial t} + \frac{\partial}{\partial x_j}(\rho' \bar{u}_j + \bar{\rho} u'_j + \rho' u'_j) = 0, \tag{18}$$

$$\frac{\partial u'_i}{\partial t} + \bar{u}_j \frac{\partial u'_i}{\partial x_j} + u'_j \frac{\partial \bar{u}_i}{\partial x_j} + u'_j \frac{\partial u'_i}{\partial x_j} = -\frac{1}{\bar{\rho}} \frac{\partial P'}{\partial x_i} \frac{1}{M^2} + \frac{\rho'}{\bar{\rho}^2} \frac{\partial (\bar{P} + P')}{\partial x_i} \frac{1}{M^2}, \tag{19}$$

$$\frac{\partial P'}{\partial t} + \bar{u}_j \frac{\partial P'}{\partial x_j} + u'_j \frac{\partial \bar{P}}{\partial x_j} + u'_j \frac{\partial P'}{\partial x_j} = -\left(\bar{P} \frac{\partial u'_k}{\partial x_k} + P' \frac{\partial \bar{u}_k}{\partial x_k} + P' \frac{\partial u'_k}{\partial x_k} \right) \gamma. \tag{20}$$

Equation (19) stipulates the balance between flow inertia on the left hand side (LHS) and the pressure forces on the right hand side (RHS). The pressure forces are inversely proportional to the square of the Mach number, indicating its reduction with increasing flow velocity. At the limit of infinite Mach number, the pressure effects can be negligible, and the momentum following a background streamline will be nearly unchanged:

$$\lim_{M \to \infty} \left[-\frac{1}{\bar{\rho}} \frac{\partial P'}{\partial x_i} \frac{1}{M^2} + \frac{\rho'}{\bar{\rho}^2} \frac{\partial (\bar{P} + P')}{\partial x_i} \frac{1}{M^2} \right] \longrightarrow 0. \tag{21}$$

This represents the pressure-released limit of flow. Clearly, the description will be valid only for a finite period of time as the integrated RHS, however small initially, will ultimately affect the momentum [2,7]. Equation (19) in the absence of the pressure terms is called the pressure-released equation for velocity perturbations. The form of Eq. (19) clearly indicates that the duration of PRE validity will increase with increasing Mach number as demonstrated in [7] for homogeneous shear flow. During the period of PRE validity, the energy equation decouples from the momentum equation as the changes in thermodynamic fluctuations are too slow to affect the velocity field evolution.

We take x, y, and z to be streamwise, normal, and spanwise directions. The background flow follows the parallel shear flow condition, and planar velocity perturbations are considered:

$$\bar{u}_i = (U(y), 0, 0), \tag{22}$$

$$u'_i = (u, v, 0). \tag{23}$$

As in the incompressible transition analysis, we restrict our considerations to planar velocity perturbations. Nonplanar and oblique perturbations will be considered in future works. Now we formulate the PRE analysis for the evolution of small perturbations in a channel flow. We linearize the equations, retaining only terms of order 1 in the perturbation field. Finally, the linearized PRE for small perturbation evolution in parallel nonuniform shear flows can be written as

$$\frac{\partial u}{\partial t} + U \frac{\partial u}{\partial x} + v \frac{dU}{dy} = 0, \tag{24}$$

$$\frac{\partial v}{\partial t} + U \frac{\partial v}{\partial x} = 0. \tag{25}$$

Perturbations that are periodic in the x direction are investigated. We take the normal mode approach [8,9] to solve the perturbation evolution equations. Normal mode forms of perturbations are given as

$$u = \hat{u}(y,t) e^{i\alpha x} + \text{c.c.}, \tag{26}$$

$$v = \hat{v}(y,t) e^{i\alpha x} + \text{c.c.} \tag{27}$$

Here $\hat{u}$ and $\hat{v}$ are the mode amplitudes of the u and v velocity perturbations, and c.c. stands for complex conjugate. The resulting mode amplitude equations are

$$\frac{D\hat{u}(y,t)}{Dt} = -\hat{v}(y,t) \frac{dU}{dy}, \tag{28}$$

$$\frac{D\hat{v}(y,t)}{Dt} = 0. \tag{29}$$

$\frac{D}{Dt}$ represents the time rate of change in the frame moving with the background flow. The mode amplitudes are clearly functions of the y coordinate and time. Therefore, the solutions to these equations will be of the form

$$\hat{u}(y,t) = \hat{u}(y,0) - \hat{v}(y,0) \frac{dU}{dy}(y) t, \tag{30}$$

$$\hat{v}(y,t) = \hat{v}(y,0). \tag{31}$$

The solution is very similar to the homogeneous shear flow PRE result, with the exception that the amplitude is dependent on the y coordinate as shear is not uniform. Given the background shear variation(dU/dy) and the initial perturbation profile $\hat{u}(y,0)$ and $\hat{v}(y,0)$, all the flow variables can be analytically determined at later times. Bertsch *et al.* [2] estimate the duration as a function of Mach number over which the PRE solution will remain a reasonable idealization of a high Mach number homogeneous shear flow. They show that the PRE result is valid for the time range [2]

$$\tau = \frac{St^*}{M^{1/2}} \sim 1.8, \tag{32}$$

where S is the local value of shear which is uniform in homogeneous shear flow. These results will be used to examine the high Mach number behavior of flow perturbations in the results section.

B. Low Mach number linear analysis

For incompressible flow, the linear analysis of small perturbation evolution is well established [8–10]. The divergence-free velocity condition decouples the momentum and energy equations. The flow can again be decomposed into background and perturbation velocities. The perturbation velocity equations are obtained by subtracting background flow equations from total flow equations:

$$\frac{\partial u'_i}{\partial x_i} = 0, \tag{33}$$

$$\frac{\partial u'_i}{\partial t} + \bar{u}_j \frac{\partial u'_i}{\partial x_j} + u'_j \frac{\partial \bar{u}_i}{\partial x_j} + u'_j \frac{\partial u'_i}{\partial x_j} = -\frac{\partial p'}{\partial x_i} + \frac{1}{\text{Re}} \frac{\partial^2 u'_i}{\partial x_j \partial x_j}. \tag{34}$$

Here the prime represents perturbation quantities and the bar represents background quantities as before. The normalization is similar to Eq. (7), except pressure is normalized in

incompressible flows as $P_0 = \rho_0 U_0^2$. The specific values of these quantities depend on the flow under consideration. For the channel flow, the reference values are those of background flow at the centerline at $t = 0$. L is half channel width. The only dimensionless parameter of relevance is the Reynolds number Re.

The background flow and perturbations are again as in Eqs. (22) and (23). This planar velocity perturbation is found to be most unstable from the linear stability theory perspective [8,9]. The perturbation equations reduce to the following forms:

$$\frac{\partial u}{\partial x} + \frac{\partial v}{\partial y} = 0, \tag{35}$$

$$\frac{\partial u}{\partial t} + U\frac{\partial u}{\partial x} = -\frac{\partial p'}{\partial x} + \frac{1}{\mathrm{Re}}\left(\frac{\partial^2 u}{\partial x \partial x} + \frac{\partial^2 u}{\partial y \partial y}\right) - v\frac{dU}{dy}, \tag{36}$$

$$\frac{\partial v}{\partial t} + U\frac{\partial v}{\partial x} = -\frac{\partial p'}{\partial y} + \frac{1}{\mathrm{Re}}\left(\frac{\partial^2 v}{\partial x \partial x} + \frac{\partial^2 v}{\partial y \partial y}\right). \tag{37}$$

In this analysis, the viscous term is retained as its effect is essential for the instability under consideration. We take a complex normal mode approach to solve the perturbation equations. Normal modes of perturbations are given as [9]

$$u = \psi(y)e^{i\alpha(x-ct)} + \text{c.c.}, \tag{38}$$

$$v = \phi(y)e^{i\alpha(x-ct)} + \text{c.c.}, \tag{39}$$

$$p' = p(y)e^{i\alpha(x-ct)} + \text{c.c.} \tag{40}$$

ψ, ϕ, and p are the complex magnitude of perturbation velocity and pressure. α is the wave number of perturbation along the streamwise direction. c is the complex phase speed. Substituting those normal mode forms into perturbation equations and combining those equations together, we can generate a single stability equation, the Orr-Sommerfeld equation (OSE)[10]. The OSE is given as

$$\frac{d^4\phi}{dy^4} - 2\alpha^2\frac{d^2\phi}{dy^2} + \alpha^4\phi - i\alpha\mathrm{Re}\left[(U-c)\left(\frac{d^2\phi}{dy^2} - \alpha^2\phi\right) - \frac{d^2U}{dy^2}\phi\right] = 0. \tag{41}$$

For channel flow, the background velocity profile is

$$U = 1 - y^2. \tag{42}$$

U is normalized with centerline velocity, and y is normalized with half channel width. With boundary conditions $y = \pm 1, \phi = \phi' = 0$, Eq. (41) reduces to an eigenvalue problem. There are many well-established procedures to solve this eigenvalue problem [11,12].

Two flow condition sets are considered in this work. For $\mathrm{Re} = 30\,406, \alpha = \pi/4$, the most unstable mode has the eigenvalue $c = 0.1734 + 0.009105i$. For $\mathrm{Re} = 45\,458, \alpha = \pi/4$, the most unstable mode has the eigenvalue $c = 0.1614 + 0.009788i$. Those corresponding eigenfunctions (ψ, ϕ) are obtained by solving the eigenvalue problem.

III. GKM: SCHEME AND SIMULATION CASES

The gas-kinetic method is emerging as a viable alternative to the NS based flow simulation scheme, especially for compressible flows. One of the potential advantages of the gas-kinetic approach over more conventional methods is that the former employs a single scalar particle distribution function f to directly compute the fluxes of mass, momentum, and energy densities [13]. The underlying argument is that it is more holistic to apply the discretization to the fundamental quantity: the distribution function f, rather than the derived quantities, the primitive or conservative variables. The constitutive relationships such as the stress tensor and heat flux vector are computed as moments of a gas distribution function on the same stencil as convective fluxes, leading to inherent consistency between various discretized conservation equations and avoiding additional viscous or conductive discretization [14]. The GKM also offers a more convenient numerical platform for including nonthermochemical equilibrium and noncontinuum effects as precise constitutive relations are not invoked in the simulations [1].

In a series of works, our research group has explored the applicability of kinetic theory based methods of the lattice Boltzmann method (LBM) and GKM to a variety of turbulent flows [1,15–20]. In [20], the authors compare the LBM and GKM against Navier-Stokes in mildly compressible turbulent flows. The GKM is augmented with a weighted essentially nonoscillatory (WENO) interpolation scheme and is examined over a large range of Mach numbers in decaying isotropic and homogeneous shear turbulence in [1].

It is important to distinguish GKM from other kinetic theory-based models such as the LBM and the direct simulation Monte Carlo (DSMC) method. LBM is a discrete velocity model wherein the different velocities at a given point represent a lattice structure on a velocity space grid. DSMC is based on conceptual particles that represent a collection of molecules. GKM, on the other hand, is a hybrid finite volume method whose details are given below.

A. GKM scheme

GKM is a finite volume numerical scheme which combines both fluid and kinetic approaches. The fluid part comes from the fact that macroscopic fluid variables are solved. The kinetic part comes from the fact that the fluxes are calculated by taking moments of a particle distribution function. The governing equation for GKM is

$$\frac{\partial}{\partial t}\int_\Omega U dx + \oint_A \vec{F}\cdot d\vec{A} = 0. \tag{43}$$

Equation (43) shows the conservation of a macroscopic flow quantity U in a control volume Ω. U represents mass, momentum, or energy. $\vec{F}$ is the flux through the cell interfaces $\vec{A}$. The GKM scheme can be decomposed into three stages: reconstruction, gas evolution, and projection. In reconstruction, the values of macroscopic variables at the cell center are interpolated to generate values at the cell interface. The WENO scheme is used for reconstruction in our solver. The WENO method is a high order accuracy interpolation scheme which also captures the steep gradients like shocks. The details of the WENO scheme are presented in [21].

In the gas evolution stage, the fluxes across the cell interface are calculated using the kinetic approach. The flux through a cell interface for the one-dimensional flow case is

$$F_1 = [F_\rho, F_{\rho v_1}, F_E]^T = \int_{-\infty}^{\infty} v_1 \psi f(x_1, t, v_1, \xi) d\Xi. \quad (44)$$

Equation (44) represents the flux calculation of mass F_ρ, momentum $F_{\rho v_1}$, and energy F_E by calculating the moments of the particle distribution function f. Here, $d\Xi = dv_1 d\xi, \xi$ is the molecular internal degrees of freedom, and ψ is the vector of moments. The expression for ψ is given by

$$\psi = \left(1, v_1, \frac{1}{2}\left(v_1^2 + \xi^2\right)\right). \quad (45)$$

To calculate f the Boltzmann equation with the Bhatnagar-Gross-Krook (BGK) collision operator is used [13]. The distribution function f is solved in the form of the following:

$$\begin{aligned} & f(x_{i+1/2}, t, v_1, v_2, v_3, \xi) \\ &= \frac{1}{\tau} \int_0^t g(x_1', t', v_1, v_2, v_3, \xi) e^{-(t-t')/\tau} dt' \\ &\quad + e^{-t/\tau} f_0(x_{i+1/2} - v_1 t). \end{aligned} \quad (46)$$

The particle distribution function f at cell interface $x_{i+1/2}$ and time t is presented in Eq. (46). Here, x_1' represents the particle trajectory, v_1, v_2. and v_3 are particle velocity space, τ is the characteristic relaxation time, f_0 is the initial distribution function, and g is the equilibrium distribution function. f_0 and g are calculated from the reconstructed macroscopic variables at the cell interface.

After f has been solved and updated, the fluxes are calculated through Eq. (44). Then in the projection stage, with calculated fluxes, Eq. (43) gives updated cell center macroscopic values.

$$U_j^{n+1} = U_j^n - \frac{1}{x_{j+\frac{1}{2}} - x_{j-\frac{1}{2}}} \int_t^{t+\triangle t} \left(F_{j+\frac{1}{2}}(t) - F_{j-\frac{1}{2}}(t)\right) dt. \quad (47)$$

Equation (47) shows the macroscopic variable updating in the one-dimensional flow case. Here, n represents the time step. The overview discussion of GKM and the full details of GKM can be found in [13].

B. Simulation cases

Temporal channel flow simulations of small perturbation evolution with a specified background velocity field are performed using the GKM. The Mach number range of the simulations is 0.08–7.2, and Reynolds number range is 30 000–230 000. The characteristic length is taken to be the channel half width, which is specified to be 0.020032 m. The domain size along the streamwise direction is considered one wavelength of perturbation. The wavelength is taken to be 8 times the channel half width. The background velocity field is parabolic and is sustained at a steady rate using a streamwise body force or pressure gradient. While both techniques yielded identical results, the body force approach was used in the final calculations for the high Mach number study as it allows the background thermodynamic state to be nearly steady. The background temperature increase due to viscous losses was found to be minimal and did not affect the outcome of the simulations even at high Mach numbers.

TABLE I. Background flow conditions for the low Mach number limit.

	U_0 (m/s)	ρ (kg/m^3)	T (K)	Re	M	grid ($x \times y \times z$)
Case 1	30	1	353	30406	0.08	$160 \times 100 \times 4$
Case 2	45	1	353	45458	0.12	$160 \times 100 \times 4$

Two channel flow cases are examined in the low Mach number study, and they are detailed in Table I. The initial perturbation profile for the low Mach number study is chosen to be the most unstable wave mode of the OSE analysis. Simulations are performed for multiple perturbation velocity amplitudes: 0.1%, 0.5%, and 2% of the background flow centerline velocity.

The high Mach number study involves three cases, the flow conditions of which are given in Table II. Following the transition to turbulence study [22], the background velocity is taken to be parabolic in shape, corresponding to a laminar flow. The PRE verification process admits any initial perturbation profile. Therefore, for the sake of simplicity, we use the low Mach number OSE solution as the perturbation profile. The streamwise wavelength and amplitude of the perturbation profile are also similar to that of the low Mach number study. In both low and high Mach number studies, the background thermodynamic field is uniform initially and evolves slowly with time. The grid resolutions are chosen based on a grid convergence investigation.

IV. RESULTS: ANALYSIS VS SIMULATIONS

The results are presented in three parts. In the first part we compare the linear analysis-based evolution of perturbation kinetic energy at low and high Mach numbers. The second part focuses exclusively on the high Mach number limit. The analytical results are compared against DNS data. A similar comparison is performed in the third part, but at the low Mach number limit.

A. Analytical results at high and low Mach number limits

At both Mach number extremes, the streamwise perturbation velocity dominates the contribution to the perturbation kinetic energy. In Fig. 1, the streamwise perturbation kinetic energy evolution as computed from linear analyses at the two Mach number extremes is plotted. The streamwise perturbation kinetic energy is calculated by performing spatial average

TABLE II. Background flow conditions for the high Mach number limit.

	U_0 (m/s)	ρ (kg/m^3)	T (K)	Re	M	grid ($x \times y \times z$)
Case 1	705.2	0.0189	61	65754	4.5	$160 \times 200 \times 4$
Case 2	931.6	0.02	60	93900	6.0	$160 \times 200 \times 4$
Case 3	1108.5	0.04	59	227763	7.2	$160 \times 200 \times 4$

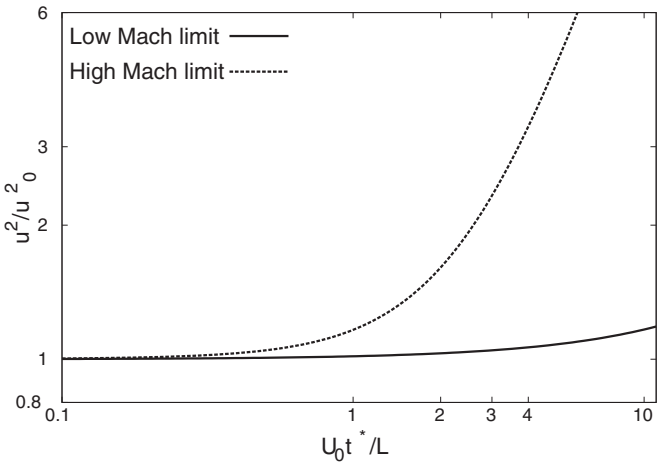

FIG. 1. Comparison of streamwise kinetic energy from linear analyses at high and low Mach number limits (low Mach number of 0.12).

along the y direction. In the absence of pressure effects, the kinetic energy grows rather rapidly in the pressure-released high Mach number limit. The low Mach number OSE solution exhibits very slow growth. It is therefore reasonable to say that the action of Poisson pressure is to significantly diminish the growth rate when compared to the pressure-released equation. This is consistent with the findings of Mishra and Girimaji [3] for homogeneous shear (Couette) flows. But it is important to note that the pressure-released effect will not last indefinitely, and consequently, the linear PRE may be valid only for a finite period of time. This will be examined by comparing linear PRE against DNS data in the next section.

B. High Mach number limit: DNS vs PRE

In Fig. 2, we compare the linear PRE results against DNS data at different Mach numbers. Nonlinear and viscous effects are present in DNS computations. The solid line in Fig. 2(a) represents the analytical PRE result obtained from squaring and integrating Eq. (30). The DNS results of various Mach numbers are shown with symbols. Clearly, the agreement is excellent at early times. It is evident that the larger Mach number simulations follow the asymptotic analytical behavior for a longer period of time, as anticipated in [2]. Next, we examine the precise duration over which the PRE formulation is valid in Fig. 2(b). Clearly, the departure of the DNS solution from PRE occurs at the estimated time τ, which has an approximate value of 1.8, the same as in [2]. Beyond this time, pressure effects begin to influence the flow field.

In the PRE analysis, the perturbation velocity field is a strong function of the wall-normal coordinate y. It is therefore important to verify whether the streamwise and wall-normal perturbation velocity profiles are captured by DNS. In Fig. 3, we compare the streamwise perturbation velocity u profile obtained from DNS data at different lapse times against the PRE solution at the corresponding times. Only the results for the Mach 6 case are shown as other cases show similar behavior. The DNS (Mach 6) results match the PRE solution at nearly all locations at all times. The numerical and analytical profiles show a small but discernible difference at the peak

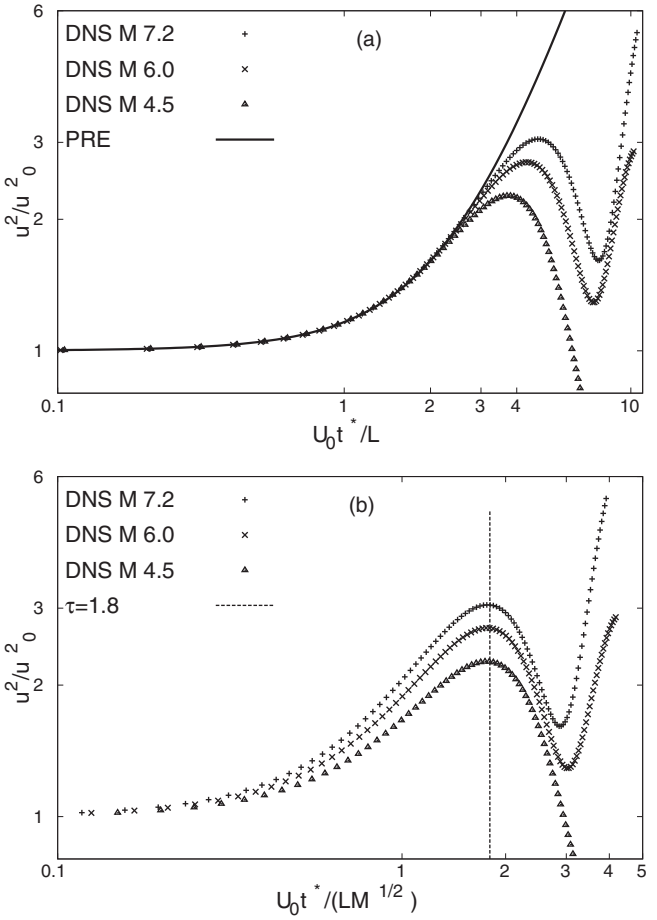

FIG. 2. DNS vs PRE for streamwise kinetic energy evolution: (a) shear time and (b) mixed time.

u locations. This observation can be attributed to the fact that peak u values occur in regions of very steep second derivatives. In these peak regions, viscous effects (second derivative) dominate over inertial effects (first derivative). Thus, the inviscid PRE solution is slightly different from the full-physics DNS solution. A comparison of DNS and PRE wall-normal perturbation velocity v profiles at different elapsed times is

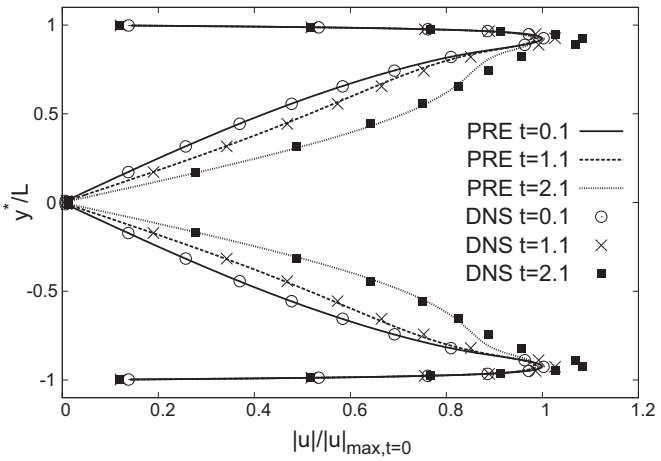

FIG. 3. Perturbation velocity u profile evolution with time at $M = 6$: $t = U_0 t^*/L$.

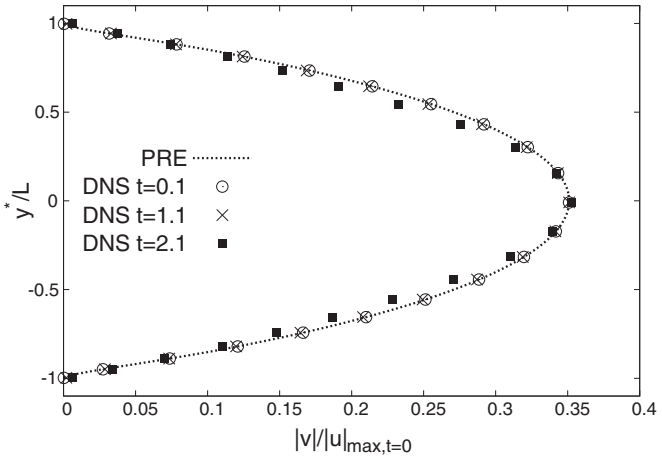

FIG. 4. Perturbation velocity v profile evolution with time at $M = 6$: $t = U_0 t^*/L$.

given in Fig. 4. The PRE analysis indicates that this profile is invariant in time. The DNS solutions do indeed capture this time independence. Overall, it is evident that the computational scheme represents the physics of the pressure-released limit accurately over the initial stages of perturbation growth; further the duration over which the DNS results are consistent with PRE is similar to that in homogeneous shear flows [1] at the high Mach number limit.

C. Low Mach number limit: DNS vs OSE

While PRE represents the asymptotic limit of pressure being too slow to modify the velocity field evolution, incompressible flow represents the opposite extreme in which pressure acts instantly to keep the velocity field divergence free at all times. We will now investigate if DNS captures the linear evolution of small perturbations as dictated by the OSE.

We commence with a comparison of DNS and OSE velocity field evolution. The DNS at two incompressible Mach numbers performed with different initial perturbation amplitudes are plotted along with OSE solutions in Fig. 5. Figure 5(a) shows case 1, for which Reynolds and Mach numbers are 30 408 and 0.08, respectively. The streamwise perturbation velocity magnitude maxima at different wall-normal distances in the DNS solution are considered. The maxima evolution for three initial intensities (0.1%, 0.5%, 2%) is found to follow the linear analysis result very closely at the early stages before nonlinear effects begin to appear. Here the time is normalized by characteristic length and initial background flow centerline velocity. In Fig. 5(b), case 2 (Re = 45 458, and $M = 0.12$) is examined. In this plot the square root of volume-averaged kinetic energy is considered. Once again, excellent agreement between the DNS results and the OSE solution is seen irrespective of the initial perturbation intensity.

Next, we compare the evolution of streamwise perturbation velocity u and wall-normal perturbation velocity v profiles in Figs. 6 and 7. Only the $M = 0.12$ (Re = 45 458) results are shown as both Mach number cases yield identical outcomes. Since the OSE solution adopts the normal mode form as (38) and (39), whose spatial and time dependency are separate, the normalized profiles of both u and v must be invariant in time.

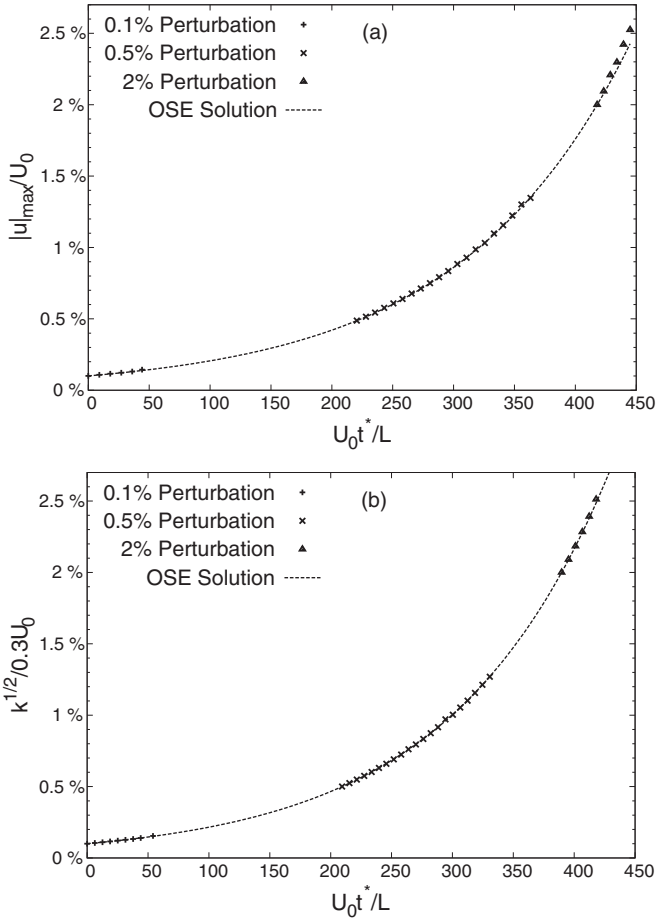

FIG. 5. Comparison of perturbation growth rate: (a) $M = 0.08$ and (b) $M = 0.12$.

Indeed, the DNS solution preserves the normal mode shape accurately.

V. SUMMARY AND CONCLUSION

We develop a linear pressure-released Navier-Stokes equation analysis to describe the stability of very high Mach number

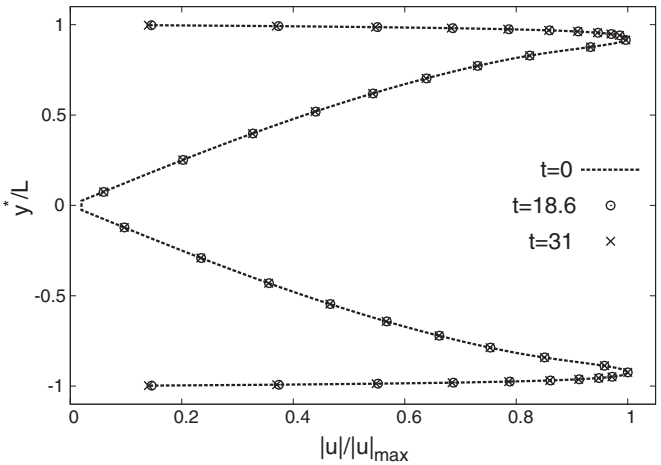

FIG. 6. Perturbation velocity u profile evolution with time at $M = 0.12$: $t = U_0 t^*/L$.

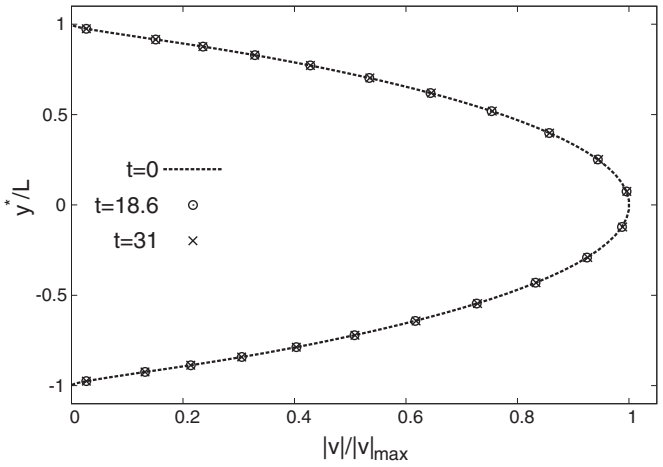

FIG. 7. Perturbation velocity v profile evolution with time at $M = 0.12$: $t = U_0 t^*/L$.

Poiseuille flow. The high speed pressure-released analysis and low speed Orr-Sommerfeld analysis are compared against Poiseuille flow simulation results at extreme Mach numbers. The numerical solver employs the gas-kinetic method to study small perturbation evolution in channel flows over a range of Mach and Reynolds numbers. The agreement between numerical simulations and linear analysis is excellent. Overall, the present study reveals the physical accuracy and numerical viability of the gas-kinetic method for simulating wall-bounded flow instabilities over a large Mach number range. Further, the importance of pressure-released analysis for describing wall-bounded nonuniform shear flow at the early stage of evolution is firmly established.

ACKNOWLEDGMENT

This work was supported by The National Center for Hypersonic Laminar-Turbulent Transition Research at Texas A&M University, NASA, and US Air Force.

[1] G. Kumar, S. Girimaji, and J. Kerimo, J. Comput. Phys. **234**, 499 (2013).
[2] R. Bertsch, S. Suman, and S. S. Girimaji, Phys. Fluids **24**, 125106 (2012).
[3] A. A. Mishra and S. S. Girimaji, J. Fluid Mech. **731**, 639 (2013).
[4] C. Cambon, G. N. Coleman, and N. N. Mansour, J. Fluid Mech. **257**, 641 (1993).
[5] R. K. Bikkani and S. S. Girimaji, Phys. Rev. E **75**, 036307 (2007).
[6] W. H. Heiser and D. T. Pratt, *Hypersonic Airbreathing Propulsion* (American Institute of Aeronautics and Astronautics, Washington, D.C., 1994).
[7] T. A. Lavin, S. S. Girimaji, S. Suman, and H. Yu, Theor. Comput. Fluid Dyn. **26**, 501 (2012).
[8] L. M. Mack, Advisory Group for Aerospace Research and Development, AGARD Report No. 1984 (unpublished).
[9] P. J. Schmid and D. S. Henningson, *Stability and Transition in Shear Flows* (Springer, New York, 2001).
[10] S. A. Orszag, J. Fluids Mech. **50**, 689 (1971).
[11] A. Davey, Q. J. Mech. Appl. Math **26**, 401 (1973).
[12] J. M. Gersting and D. F. Jankowski, Int. J. Numer. Meth. Eng. **4**, 195 (1972).
[13] K. Xu, L. Martinelli, and A. Jameson, J. Comput. Phys. **120**, 48 (1995).
[14] G. May, B. Srinivasan, and A. Jameson, J. Comput. Phys. **220**, 856 (2007).
[15] H. Yu, L. Luo, and S. S. Girimaji, Int. J. Comput. Eng. Sci. **03**, 73 (2002).
[16] H. Yu, S. S. Girimaji, and L. Luo, J. Comput. Phys. **209**, 599 (2005).
[17] H. Yu, S. S. Girimaji, and L. S. Luo, Phys. Rev. E **71**, 016708 (2005).
[18] D. Yu and S. S. Girimaji, Phys. A (Amsterdam, Neth.) **362**, 118 (2006).
[19] H. Yu and S. S. Girimaji, Phys. Fluids **17**, 125106 (2005).
[20] J. Kerimo and S. S. Girimaji, J. Turbul. **8**, N46 (2007).
[21] G. Jiang and C. Shu, J. Comput. Phys. **126**, 202 (1996).
[22] C. Liang, S. Premasuthan, A. Jameson, and Z. J. Wang, *47th AIAA Aerospace Sciences Meeting including The New Horizons Forum and Aerospace Exposition, AIAA Paper 2009-402, Orlando, Florida, January 5–8, 2009* (AIAA, Reston, VA, 2009).